NANO · MICRO small
www.small-journal.com

High Density Single Fe Atoms on Mesoporous N-Doped Carbons: Noble Metal-Free Electrocatalysts for Oxygen Reduction Reaction in Acidic and Alkaline Media

Haifang Xie, Bing Du, Xiaoxi Huang, Dahai Zeng, Hui Meng, Huaijun Lin, Wei Li, Tewodros Asefa, and Yuying Meng**

It remains a challenge to develop efficient noble metal-free electrocatalysts for the oxygen reduction reaction (ORR) in various renewable energy systems. Single atom catalysts have recently drawn great attention as promising candidates both due to their high activity and their utmost atom utilization for electrocatalytic ORR. Herein, the synthesis of an efficient ORR electrocatalyst that is composed of N-doped mesoporous carbon and a high density (4.05 wt%) of single Fe atoms via pyrolysis Fe-conjugated polymer is reported. Benefiting from the abundant atomic Fe–N_4 sites on its conductive, mesoporous carbon structures, this material exhibits an excellent electrocatalytic activity for ORR, with positive onset potentials of 0.93 and 0.98 V in acidic and alkaline media, respectively. Its electrocatalytic performance for ORR is also comparable to that of Pt/C (20 wt%) in both media. Furthermore, it electrocatalyzes the reaction almost fully to H_2O (or barely to H_2O_2). Additionally, it is durable and tolerates the methanol crossover reaction well. Furthermore, a proton exchange membrane fuel cell and a zinc–air battery assembled using it on their cathode deliver high maximum power densities (320 and 91 mW cm^{-2}, respectively). Density functional theory calculation reveals that the material's decent electrocatalytic performance for ORR is due to its atomically dispersed Fe–N_4 sites.

1. Introduction

The growing global demand of energy and the over-consumption and negative environmental impacts of fossil fuels continue to call for environmental-friendly and sustainable energy technologies, such as proton exchange membrane fuel cells (PEMFCs) and metal–air batteries.[1] In these promising sustainable energy systems, the oxygen reduction reaction (ORR), which takes place at their cathode electrodes, is the most crucial process that governs their overall performances.[2] However, as this reaction involves a sluggish 4-electron transfer kinetics, it can consume a large amount of energy without the right electrocatalyst. At present, noble metals, especially platinum (Pt) and its oxides, are used as the state-of-the-art electrocatalysts for it because they can reduce the overpotential of the reaction and drive it with less energy consumption. Unfortunately, the large-scale application of these noble metal-based catalysts is challenging due to their high cost, limited reserves in the Earth's crust, poor durability, and poor tolerance to the methanol crossover reaction.[3] Therefore, it is of high importance to explore and develop alternative, noble metal-free ORR electrocatalysts that are cost-effective and stable in both acidic and alkaline media.

Among various noble metal-free candidate electrocatalysts, transition metal single-atom catalysts (SACs) have recently raised tremendous interest because they allow for almost 100% atom utilization as well as because they offer uniformly dispersed metallic active sites.[4] Particularly, single metal atoms coordinated with nitrogen ligands on N-doped carbons (in form of M-N-C, where M is Fe, Co, Ni, Cu, etc.) have been found to exhibit encouraging

H. Xie, D. Zeng, H. Lin, W. Li, Y. Meng
Institute of Advanced Wear & Corrosion Resistant and Functional Materials
Jinan University
601 Huangpu Avenue West, Guangzhou 510632, China
E-mail: yymeng9169@jnu.edu.cn

B. Du
College of Materials Science and Engineering
Shenzhen University
1066 Xueyuan Avenue, Shenzhen 518060, China

The ORCID identification number(s) for the author(s) of this article can be found under https://doi.org/10.1002/smll.202303214

DOI: 10.1002/smll.202303214

X. Huang
Hoffmann Institute of Advanced Materials, Postdoctoral Innovation Practice Base
Shenzhen Polytechnic
7098 Liuxian Blvd, Nanshan District, Shenzhen 518055, China

H. Meng
College of Science and Engineering
Jinan University
601 Huangpu Avenue West, Guangzhou 510632, China

T. Asefa
Department of Chemistry and Chemical Biology & Department of Chemical and Biochemical Engineering, Rutgers, 610 Taylor Road
The State University of New Jersey
Piscataway, NJ 08854, USA
E-mail: tasefa@chem.rutgers.edu

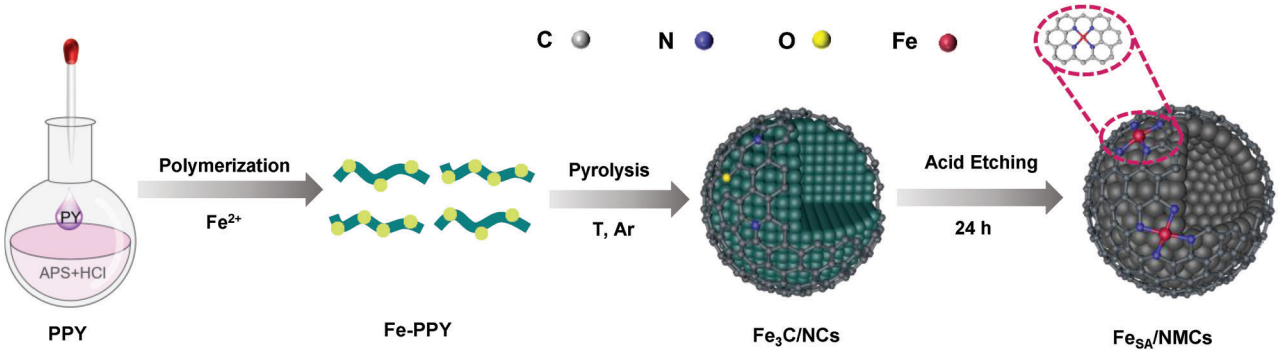

Scheme 1. Schematic illustration of the synthetic procedure leading to single Fe atoms anchored onto N-doped mesoporous carbon (Fe_{SA}/NMCs). The procedure involves the preparation of Fe-chelated PPY (Fe-PPY), followed by the pyrolysis of Fe-PPY, and subsequently the acid treatment of the pyrolyzed material to etch Fe_3C byproduct from it. The abbreviations PY, APS, and Fe-PPY represent pyrrole, ammonium persulfate, and Fe-chelated polypyrrole.

catalytic activity and selectivity for ORR because of their conductivity and tunable electronic structures.[5] For example, isolated Fe–N_x moieties anchored onto carbon materials were reported to electrocatalyze ORR in alkaline electrolyte well.[6] However, the performances of these single atom sites in acidic electrolyte is still unsatisfactory and requires further improvement to expedite their practical applications. As the activity of such electrocatalysts is directly related to the density of their active sites, increasing the overall density and the accessibility of these atomically dispersed Fe–N_x moieties is one possible way to improve their overall activity.[7] But, this is still challenging to achieve because of the inherent tendency of isolated single metal atoms to aggregate and form clusters or nanoparticles during high temperature pyrolysis.[8] Consequently, extensive studies are ongoing to develop synthetic methods that can increase the density of isolated single Fe atoms on catalysts to a satisfactory loading (typically 4 wt% or more).[9]

In this work, we report the synthesis of efficient ORR electrocatalysts composed of N-doped mesoporous carbons containing a high density of single Fe atoms (denoted as Fe_{SA}/NMCs) via pyrolysis of Fe-containing polypyrrole (Fe-PPY) at high temperatures and then removing the Fe_3C byproducts formed in them with an acidic solution. The removal of Fe_3C also introduces mesopores and exposes more atomic Fe–N_4 sites within the materials, thereby rendering them highly electrocatalytically active. The most optimal material is obtained by pyrolysis of the precursor at 800 °C (Fe_{SA}/NMCs-800), and it possesses 4.05 wt% single Fe atoms or a relatively high loading compared with those of many related systems. The material exhibits excellent electrocatalytic performances toward ORR in both acidic and alkaline media, with onset potentials of 0.93 and 0.98 V, respectively. Its performances are also comparable to those of a commercially available Pt/C (20 wt%) electrocatalyst. In addition, it is more durable and tolerant to the methanol crossover reaction than Pt/C (20 wt%) during the reaction. Its good electrocatalytic activities are attributed to its high density of well-dispersed Fe–N_4 sites, N dopants, and mesoporous structures. A proton exchange membrane fuel cell (PEMFC) and a zinc–air battery assembled using Fe_{SA}/NMCs-800 as electrocatalyst show decent performances, as well, with high peak power densities of 320 and 91 mW cm^{-2}, respectively, indicating the potential applications of the electrocatalyst in practical renewable energy conversion and storage devices.

2. Results and Discussion

Briefly, Fe_{SA}/NMC-800 is synthesized by preparing and then pyrolyzing Fe-PPY that contains Fe^{2+}-to-pyrrole mole ratio (or R) of 1/2 at 800 °C under inert (Ar) atmosphere, and subsequently removing the Fe_3C particles trapped within the pyrolyzed material using an acidic solution at room temperature. The procedure is illustrated in **Scheme 1** and in the Supporting Information. For comparison, a series of Fe_{SA}/NMC-T materials are synthesized by preparing Fe-PPY with the same mole ratio and then pyrolyzing it at different temperatures, in between 600 and 900 °C. Similarly, a series of Fe_{SA}/NMC-R materials are synthesized by pyrolyzing at 800 °C of Fe-PPY prepared with different R, namely 1/8, 1/4, 1/2, and 1/1. Additionally, for comparison, Fe-free N-doped carbon black (NCB) is synthesized from PPY with the same procedure. The synthetic details are provided in the Experimental Section and Table S1 in the Supporting Information.

X-ray diffraction (XRD) pattern of the pyrolyzed product synthesized at 800 °C before acid treatment, which is named Fe_3C/NC-800, displays several sharp peaks associated with crystalline Fe_3C and a broad peak (at ≈26.2°) corresponding to graphitic carbon (**Figure 1**a).[10] In the case of XRD pattern of the acid-treated material, the diffraction peaks associated with Fe_3C are no longer observed, and only two broad peaks at 26.2° and 44.3°, which can be indexed as the (002) and (101) lattice planes of graphite-2H (PDF#41-1487),[11] respectively, are seen. This indicates the complete removal of Fe_3C from the material. In the XRD patterns, no peaks associated with Fe are also detected, indicating the absence of crystalline Fe particles. The XRD patterns of all Fe_{SA}/NMC materials and the control material NCB (Figure S1, Supporting Information) show only two diffraction peaks at ≈26.2° and 44.3°, which are characteristic of graphitic carbon. It is worth noting that peaks corresponding to Fe or Fe carbides are not discerned in the XRD patterns of all Fe_{SA}/NMC materials. This must be due to the atomic dispersion of the Fe-species, as confirmed by other methods below.

Scanning electron microscope (SEM) and transmission electron microscopy (TEM) images of Fe_3C/NC-800, Fe_{SA}/NMC-800, and NCB are obtained to investigate the morphologies and structures of the materials. In the SEM images of these three materials, interconnected nanospheres with diameters in the range of 100–200 nm are observed (Figure S2, Supporting

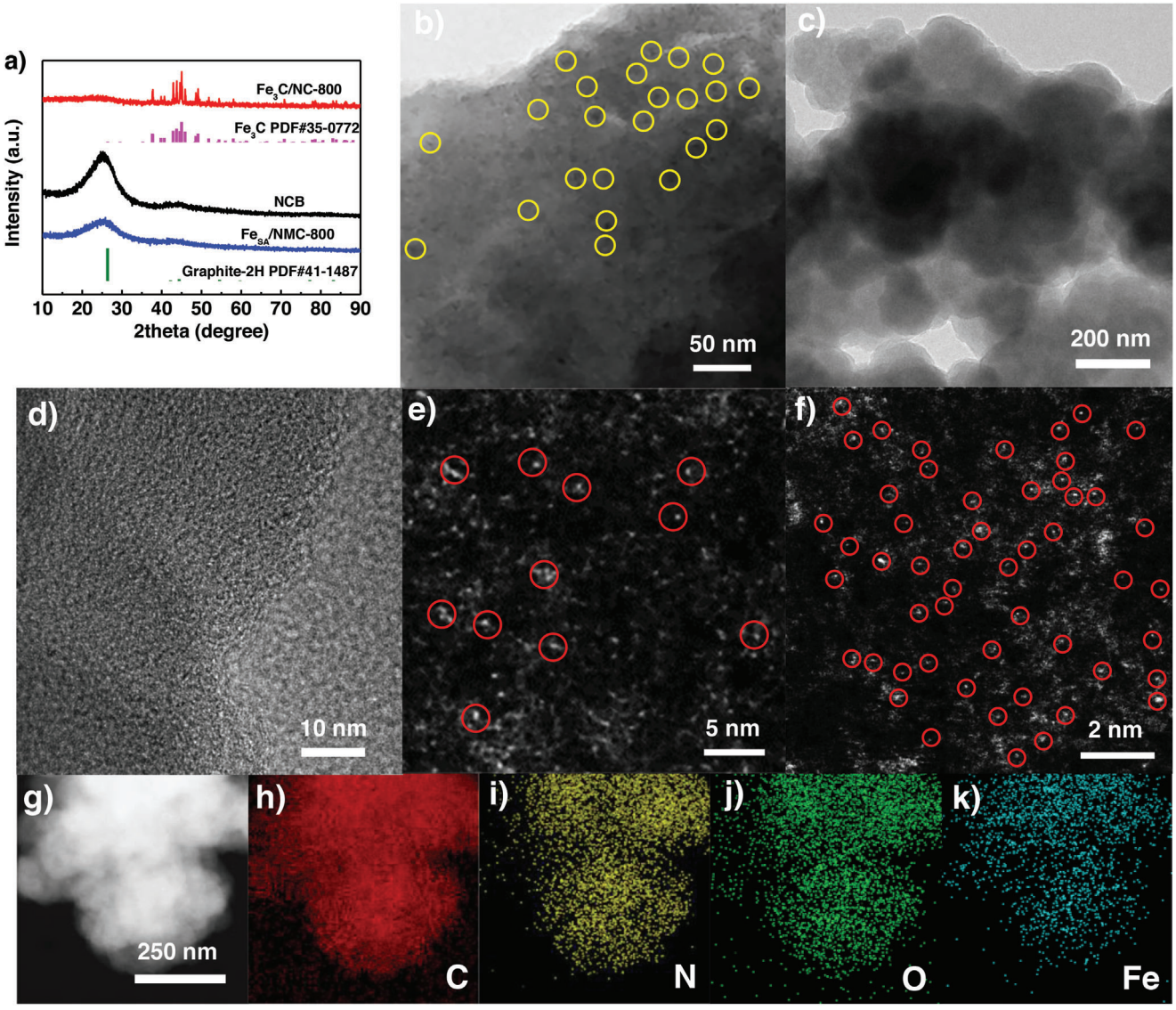

Figure 1. a) XRD patterns of Fe_{SA}/NMC-800, Fe_3C/NC-800, and NCB materials. TEM images of b) Fe_3C/NC-800 and c) Fe_{SA}/NMC-800. d) HR-TEM image; e,f) AC HAADF-STEM image (in which isolated Fe active sites are highlighted with yellow circles); and g) STEM image of Fe_{SA}/NMC-800 and the corresponding elemental mapping images of h–k) Fe, N, O, and C, respectively.

Information). TEM image of Fe_3C/NC-800 (i.e., the pyrolyzed material before acid treatment) displays some dark spots corresponding to nanoparticles, which are highlighted with yellow circles in the image in Figure 1b. These dark spots, which have sizes in the range of 4–8 nm (see Figure S3, Supporting Information), must be the Fe_3C nanoparticles that were detected by XRD. Additional TEM and high-resolution TEM (HR-TEM) images of Fe_3C/NC-800 are shown in Figure S4b,c (Supporting Information). The HR-TEM images of the material exhibit two sets of lattice fringes with spacings of 0.240 and 0.227 nm, which can be indexed as the (210) and (002) crystallographic planes, respectively, of Fe_3C (Figure S4c, Supporting Information).[12] The elemental mapping images of the material taken from the region of the high-angle annular dark field (HAADF) images (Figure S4d–h, Supporting Information) show C, N, O, and Fe that are uniformly distributed throughout the interconnected particles, indicating the homogeneous dispersion of Fe_3C nanoparticles on N-doped carbon matrices. The TEM image of the material after treatment with an acidic solution (i.e., Fe_{SA}/NMC-800) shows only carbon nanospheres with smooth surfaces (Figure 1c). Notably also, the image does no longer show Fe_3C nanoparticles, indicating their removal by the acidic solution. HR-TEM image of this material (Figure 1d) merely shows amorphous carbon with poor crystallinity and short-range order, further corroborating the removal of Fe_3C or the absence of Fe nanoparticles. These observations are all in accordance with the XRD results discussed earlier. The absence of Fe nanoparticles implies that the possible aggregation of Fe atoms into nanoparticles/clusters during the pyrolysis process step must have been inhibited, possibly due to the coordination of the Fe species in the materials

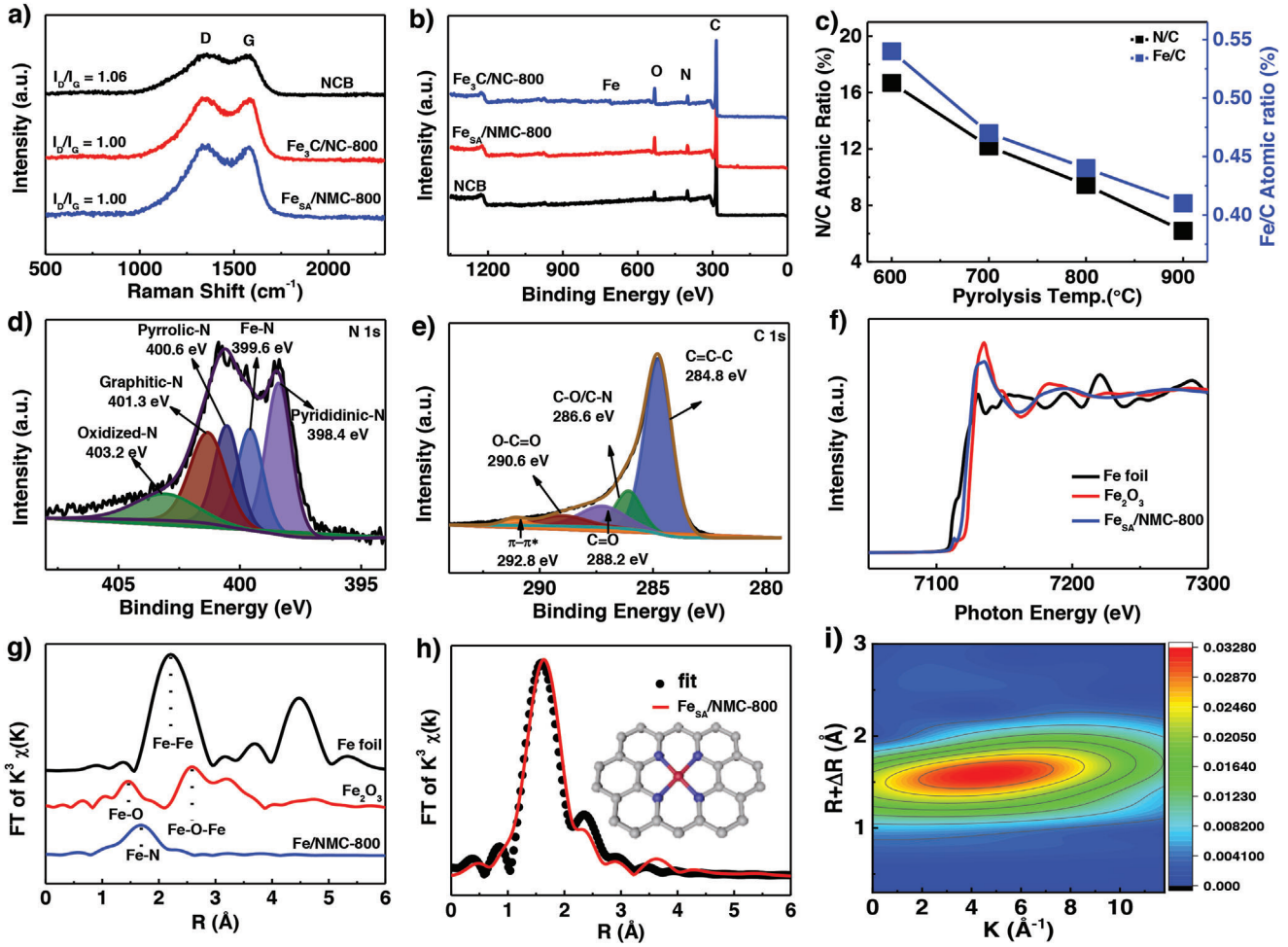

Figure 2. a) Raman spectra and b) XPS survey spectra of Fe_3C/NC-800, Fe_{SA}/NMC-800, and NCB. c) Atomic ratios of N:C and Fe:C in Fe_{SA}/NMC-T materials as a function of the pyrolysis temperature used to synthesize them. High-resolution XPS spectra of d) N 1s and e) C 1s peaks of Fe_{SA}/NMC-800. f) Normalized Fe-K edge XANES spectra and g) FT of k^3-weighted EXAFS spectra of Fe_{SA}/NMC-800, Fe foil, and Fe_2O_3. h) EXAFS spectrum of Fe K-edge, along with *R*-space filling curve, is shown. The inset shows the schematic model of Fe coordination environment on the material, where the color representations are: red is for Fe, blue is for N, and gray is for C. i) WT EXAFS spectra of Fe_{SA}/NMC-800.

with the N sites in PPY (i.e., the polymer used to produce the N-doped carbon material) in the form of Fe-PPY.

Fe_{SA}/NMC-800 is examined further with an aberration-corrected high-angle annular dark-field scanning transmission electron microscope (AC HAADF-STEM) to acquire atomic level compositional information about it (Figure 1e,f). In the images, no Fe-based crystalline nanoparticles or clusters are seen, while numerous isolated Fe single atoms on the carbon matrix (highlighted with red circles in the images) are observed. Elemental mapping images show a homogeneous dispersion of C, N, O, and Fe species (Figure 1g–k), and highly dispersed Fe sites over the entire carbon material. The single Fe atoms must be largely coordinated to the N dopant atoms on the carbon framework in form of Fe–N_x (as discussed below).[13] The amount of supported single Fe atoms on Fe_{SA}/NMC-800 is determined to be 4.05 wt% by inductively coupled plasma optical emission spectrometry (ICP-OES). This value is larger than those reported for other single Fe atoms-doped carbon materials (Table S2, Supporting Information).[14] N_2 adsorption–desorption isotherm of Fe_{SA}/NMC-800 is obtained to determine its porosity and pore properties. Its surface area, which is calculated by the Brunauer–Emmett–Teller (BET) method, is 386 m^2 g^{-1}, and its average pore diameter, which is determined by the Barrett–Joyner–Halenda (BJH) method, is ≈6.5 nm (Figure S5a,b, Supporting Information). The pores in the material are largely formed from the removal of Fe_3C nanoparticles, as the parent material with these nanoparticles is largely devoid of such pores (Figure S5c,d, Supporting Information). The large surface area and mesoporous structures of Fe_{SA}/NMC-800 can be expected to expose the single Fe atoms in it to reactants, facilitate the mass transfer of reactants and products within its structure, and increase the overall activity of the material during catalysis.[6d]

The Raman spectra of Fe_{SA}/NMCs, Fe_3C/NC-800, and NCB materials (Figure 2a; and Figure S6, Supporting Information) exhibit two distinct peaks at ≈1344 and 1580 cm^{-1}, which can be assigned to the D band (structural defects) and the G band (graphitic structures) of carbon materials, respectively.[8c] The ratio of the intensities of D and G peaks in the Raman spectrum

(I_D/I_G) of Fe_{SA}/NMC-800 is smaller (≈1.00) than that of NCB (≈1.06), indicating that the former has more graphitic structure. This might be because of the Fe species present in the former, which are known to promote the formation of graphitic carbon during pyrolysis of carbon precursors at high temperature.[15] Meanwhile, the value of I_D/I_G of Fe_{SA}/NMC-800 is like that of Fe_3C/NC-800 (≈1.00), indicating that the etching of Fe_3C particles does not lead to additional structural defects in the carbon framework. In the case of Fe_{SA}/NMC-T materials, the value of I_D/I_G decreases from 1.05 to 0.96 as the pyrolysis temperature used to produce them is increased from 600 to 900 °C (Figure S6c, Supporting Information). This is not surprising given the fact that higher pyrolysis temperature helps carbon materials undergo more graphitization.[16] However, in the case of Fe_{SA}/NMC-R materials, their I_D/I_G ratio increases gradually as the amount of Fe^{2+} in their precursor is increased, or as the value of *R* is raised from 1/8 to 1/1. This means increasing the amount of Fe^{2+} ions in the precursor more and more rather leads to a higher value of I_D/I_G, or a more disordered carbon structure with the extra Fe species going to form aggregated Fe particles that are later removed by the acidic solution (as discussed further below). These results indicate that a moderate amount of Fe species is necessary to facilitate the degree of graphitization of the carbon matrix while leaving behind the highest possible amount of single atom Fe sites.[15]

X-ray photoelectron spectroscopy (XPS) is used to examine the materials' surface compositions and chemical states. The survey XPS spectrum of Fe_3C/NC-800, which is displayed in **Figure 2**b, confirms the presence of C, N, O, and Fe in the material. The XPS spectrum of Fe_{SA}/NMC-800 does not show peaks corresponding to Fe due to the low content of Fe species in the material after the treatment with an acidic solution (Figure S7, Supporting Information). It still shows the peaks that are characteristic of C, N, and O, though. The amounts of surface N dopants in Fe_3C/NC-800 and Fe_{SA}/NMC-800 are 7.97 and 7.89 at%, respectively (see Table S3, Supporting Information). Both are slightly higher than that of NCB, which is 7.70 at%. The higher amount of N in the former two materials could be because of the ability of the Fe atoms in them to coordinate with the N species in PPY, inhibiting the loss of N atoms from the carbon framework during the pyrolysis of their precursors.[16b] Meanwhile, the treatment of the materials with an acidic solution removes Fe_3C, along with some N dopants, making the amount of N in them relatively lower.

In the case of pyrolysis temperature, when it is increased from 600 to 900 °C, the N:C atomic ratios of Fe_{SA}/NMC-T materials decrease from 0.16 to 0.06 (Figure 2c). This must be due to the loss of more N atoms when higher pyrolysis temperature is used, which is in accordance with the results previously reported for related materials.[17] At the same time, the Fe:C atomic ratios of Fe_{SA}/NMC-T materials decrease, from 0.5% to 0.4%, because the loss of more N at higher pyrolysis temperatures makes more Fe to form Fe carbides that then get removed by the acidic solution. On the other hand, the Fe:C atomic ratios increase from 0.30% to 0.45%, as the value of *R* increases from 1/8 to 1/1 (which corresponds to an increase in the relative amount of Fe^{2+} ions in Fe-PPY) (Figure S8, Supporting Information). It is also noteworthy that the N:C atomic ratios of Fe_{SA}/NMC-R materials increase when higher values of *R* are used for their synthesis. For example, when *R* is increased from 1/8 to 1/2, the N:C atomic ratio increases from 7.29 to 9.45%; however, when *R* is increased further, from 1/2 to 1/1, the N:C atomic ratio remains almost the same (≈ 9.45%). This means excess amounts of Fe^{2+} ions do not lead to more Fe–N_x moieties or a higher amount of N dopants in the materials, but they rather lead to Fe aggregates, as discussed earlier and as observed in the TEM images of these materials (see Figure S22, Supporting Information). The amount of Fe on the surfaces of Fe_{SA}/NMC-800, which is determined by XPS analysis, is ≈0.37 at% (≈1.6 wt%). This is much lower than the total amount of Fe in this material, which is determined by ICP-OES and which is ≈4.05 wt%. This indicates that the Fe atoms are dispersed not only over the surfaces but also in the entire structures of the carbon matrix.

High-resolution XPS spectra of N 1s peaks of Fe_{SA}/NMC-800 and the other Fe_{SA}/NMC materials are deconvoluted into five peaks, as depicted in Figure 2d; and Figures S9 and S10 (Supporting Information). The peaks correspond to pyridinic-N (at 398.4 eV), Fe-coordinated N (Fe–N) (at 399.6 eV), pyrrolic-N (400.6 eV), graphitic-N (at 401.3 eV), and oxidized-N (at 403.2 eV) species.[5b,6d] The peak associated with Fe–N species indicates that Fe atoms are coordinated with N atoms in the carbon material with Fe–N_x configuration. These five peaks are also detected in the XPS spectrum Fe_3C/NC-800 (Figure S11, Supporting Information). Based on high-resolution XPS spectra of N 1s peak, the amounts of surface Fe–N_x species in Fe_3C/NC-800 and Fe_{SA}/NMC-800 are found to be almost the same, ≈21 at% of the total amount of N. This indicates that the Fe-N_x species in the materials remain the same before and after acid treatment. It also indicates that the Fe–N_x species in the materials are acid resistant. The XPS spectra of C 1s of Fe_{SA}/NMCs, Fe_3C/NC-800, and NCB (Figure 2e; and Figures S12–S14, Supporting Information) are fitted into five peaks, corresponding to C=C–C (284.8 eV), C–N/C–O (286.6 eV), C=O (288.2 eV), O–C=O (290.6 eV), and π–π^* (292.8 eV) species.[15a] Meanwhile, high-resolution spectrum of Fe 2p of Fe_3C/NC-800 (Figure S15, Supporting Information) shows peaks at 711.1 and 724.0 eV that can be assigned to Fe^{2+} species as well as peaks at 715.2 and 728.4 that are attributable to Fe^{3+} species.[12a]

Synchrotron X-ray absorption spectroscopy is used to uncover the local coordination environments and electronic structures of Fe sites in the materials.[18] The X-ray absorption near-edge structure (XANES) spectra of Fe at K-edge (Figure 2f) of Fe_{SA}/NMC-800 shows a peak that falls in between those of Fe foil and Fe_2O_3, i.e., the two reference systems used for this spectral study. The results also show the valence states of Fe in Fe_{SA}/NMC-800 are between 0 and +3. This indicates that the Fe sites in the material are not only positively charged but also coordinated with N atoms.[19] The Fourier-transformed (FT) k^3-weighted Fe K-edge extended X-ray absorption fine structure (EXAFS) profile of Fe_{SA}/NMC-800 (Figure 2g) reveals a major peak at ≈1.69 Å in *R* space corresponding to scattering associated with Fe–N or Fe–O moieties, but no peak at ≈2.2 Å corresponding to Fe–Fe interactions.[20] This means that single Fe atoms in the form of isolated Fe–N or Fe–O moieties are dominant in Fe_{SA}/NMC-800. This is in line with the results obtained with AC HAADF-STEM imaging earlier. Since the Fourier transform spectra cannot distinguish between Fe–N and Fe–O configurations, due to their close interatomic distances, wavelet-transform (WT) EXAFS analysis is performed to identify the backscattering atoms (Figure 2i). The

maximum WT intensity for Fe_{SA}/NMC-800 is seen at ≈4.5 $Å^{-1}$ in *k*-space, indicating the prevalence of Fe–N coordinated species in the material.[6b,21] The fitted EXAFS result and quantitative analysis show that the average coordination number (*N*) of Fe_{SA}/NMC-800 is 3.5, with *R*-factor of 0.028 (Figure 2h; and Table S4, Supporting Information), verifying the presence/formation of Fe–N_4 coordinated sites in the material (see inset in Figure 2h). The above observations collectively indicate that the Fe atoms in this material are atomically dispersed onto the mesoporous N-doped carbon matrix with Fe–N_4 configuration. It is also worth adding here that such Fe–N_4 sites are among the most active electrocatalytic sites for ORR.[5b,7a]

The electrocatalytic properties and performances of Fe_{SA}/NMCs, Fe_3C/NC-800, and the control material Fe-free N-doped carbon black (NCB) for ORR are then evaluated by measuring current density of the reaction versus potential with a potentiostat. The first tests are done in 0.1 M $HClO_4$ solution at room temperature using a three-electrode cell configuration comprised of a saturated calomel electrode (SCE) and a graphite rod as reference and counter electrodes, respectively. All the measured potentials are recorded with respect to reversible hydrogen electrode (RHE) after its calibration (Figure S16, Supporting Information). The cycle voltammetry (CV) curve for Fe_{SA}/NMC-800 in O_2-saturated electrolyte shows a distinct cathodic peak at a potential of 0.67 V (vs RHE), but the curve obtained for the same material in Ar-saturated electrolyte shows no peak within the same potential window (Figure S17, Supporting Information), indicating that the material is electrocatalytically active toward ORR in acidic medium.[22]

Linear sweep voltammetry (LSV) curve acquired for Fe_{SA}/NMC-800 with a rotating disk electrode (RDE) (**Figure 3**a) confirms its excellent activity for ORR. Its onset potential (E_{onset}), half-wave potential ($E_{1/2}$), and limiting diffusion current density (J_L) at rotational speed of 1600 rpm are 0.93, 0.71 V, and 5.75 mA cm^{-2}, respectively. These values are comparable to those of a commercially available Pt/C (20 wt%), whose corresponding values are E_{onset} = 0.94 V, $E_{1/2}$ = 0.74 V, and J_L = 5.75 mA cm^{-2} (Figure S18a, Supporting Information). The material's electrocatalytic activity also outperforms those of some notable previously reported carbon-based transition-metal single atom electrocatalysts for ORR in acidic media (see Table S5, Supporting Information).[23] Besides, the Tafel slope of the reaction is found to be 68 mV dec^{-1} (Figure 3b), which is comparable to that of Pt/C (20 wt%), which is 63 mV dec^{-1} (Figure S18b, Supporting Information). This indicates that the kinetics of ORR over Fe_{SA}/NMC-800 in a small current density region is fast.[4c] While NCB can also electrocatalyze ORR, its activity is relatively poor, with more negative onset potential, larger Tafel slope, and smaller limiting diffusion current density compared with Fe_{SA}/NMC-800. This indirectly indicates that the electrocatalytic activity of Fe_{SA}/NMC-800 is largely due to the Fe single atoms or Fe–N_4 sites, rather than the underlying carbon material. While Fe_3C/NC-800 electrocatalyzes ORR with almost the same onset and half-wave potentials as Fe_{SA}/NMC-800, it does so with a smaller limiting diffusion current density (J_L = 5.2 mA cm^{-2}). Since both materials have similar amounts of Fe–N_4 species, the larger value of J_L of Fe_{SA}/NMC-800 can be attributed to its larger BET surface area and more accessible Fe–N_4 species, due to the mesopores formed in it upon the removal of Fe_3C nanoparticles. This is further corroborated by the larger electrochemically active surface area (ECSA) of Fe_{SA}/NMC-800 obtained for it, which is 385 cm^2, compared with those of NCB and Fe_3C/NC-800, which are 37 and 243 cm^2, respectively (see the Experimental Section in Supporting Information and Figure S19, Supporting Information). The kinetic current density (J_K) at a chosen potential of 0.6 V for the reaction over Fe_{SA}/NMC-800 is calculated to be 41 mA cm^{-2} (Figure S20, Supporting Information), which is also high, corroborating its excellent electrocatalytic activity for ORR.

LSV curves of ORR over the materials obtained at various rotating speeds (from 400 to 2400 rpm) show that the current density of the reaction increases as the electrode's rotating speed increases (Figure 3c). This is obviously due to the improved diffusion of O_2 in the electrolyte as well as around the electrode as the electrode rotates faster.[24] The Koutecky–Levich (*K–L*) or J^{-1} versus $\omega^{-1/2}$ plots (Figure 3d), which are derived from polarization curves obtained with RDE at different rotating rates, reveal a linear relationship in a wide potential range (0.1–0.7 V). This indicates that the kinetics of ORR over the materials with respect to the concentration of dissolved O_2 is first order. The electron transfer number (*n*) per O_2 molecule involved in the reaction, which is calculated based on the *K–L* equation, is ≈4.0 (Figures S20–S25, Supporting Information). This shows that ORR takes place over Fe_{SA}/NMC-800 through a more desirable 4-electron reduction pathway. This also means that Fe_{SA}/NMC-800 drives the electrocatalytic reduction of O_2 molecules in acidic solution to water. This is further corroborated by a measurement made with rotating ring-disk electrode (RRDE) technique at speed of 1600 rpm over this catalyst in the potential range of 0.07–0.8 V. From this experiment, a low yield (<2%) of H_2O_2, which is a partial (2-electron) reduction product of ORR, as well as a value of *n* close to 4 is obtained (Figure 3c), matching well with the one obtained based on the *K–L* plots earlier. All these results demonstrate that Fe_{SA}/NMC-800 electrocatalyzes ORR in acidic medium through a 4-electron pathway, almost exclusively producing H_2O.

Next, the effects of pyrolysis temperature and the amount of Fe loaded in Fe_{SA}/NMC materials on the electrocatalytic activities of the materials toward ORR are investigated. In the case of Fe_{SA}/NMC-T, a volcano trend of catalytic activity versus pyrolysis temperature is observed. More specifically, when the pyrolysis temperature of the materials is raised from 600 to 800 °C, their onset potentials to catalyze the reaction at rotational speed of 1600 rpm is shifted to a positive value, from 0.80 to 0.93 V, while their limiting diffusion current density increases from 4.34 to 5.75 mA cm^{-2} (Figure S21a, Supporting Information). This can be attributed to the increase in the degree of graphitic carbon in the materials, as evidenced from the decrease in their I_D/I_G ratios, from 1.05 to 1.00. However, as the pyrolysis temperature is further raised to 900 °C, the limiting diffusion current density slightly decreases. This might be because the Fe atoms on the materials form more aggregates/clusters or nanoparticles on the materials at higher pyrolysis temperatures (Figure S22, Supporting Information) that are then removed by the acidic solution, leaving behind a lower density of catalytically active Fe–N_4 sites.[8b,25] In the case of Fe_{SA}/NMC-R materials, the same type of volcano trend between limiting diffusion current density versus *R* (i.e., the amount of Fe^{2+} ions:PPY used for synthesis of the materials) is also observed (Figure S21b, Supporting Information). In this case, the current density of the reaction over the materials

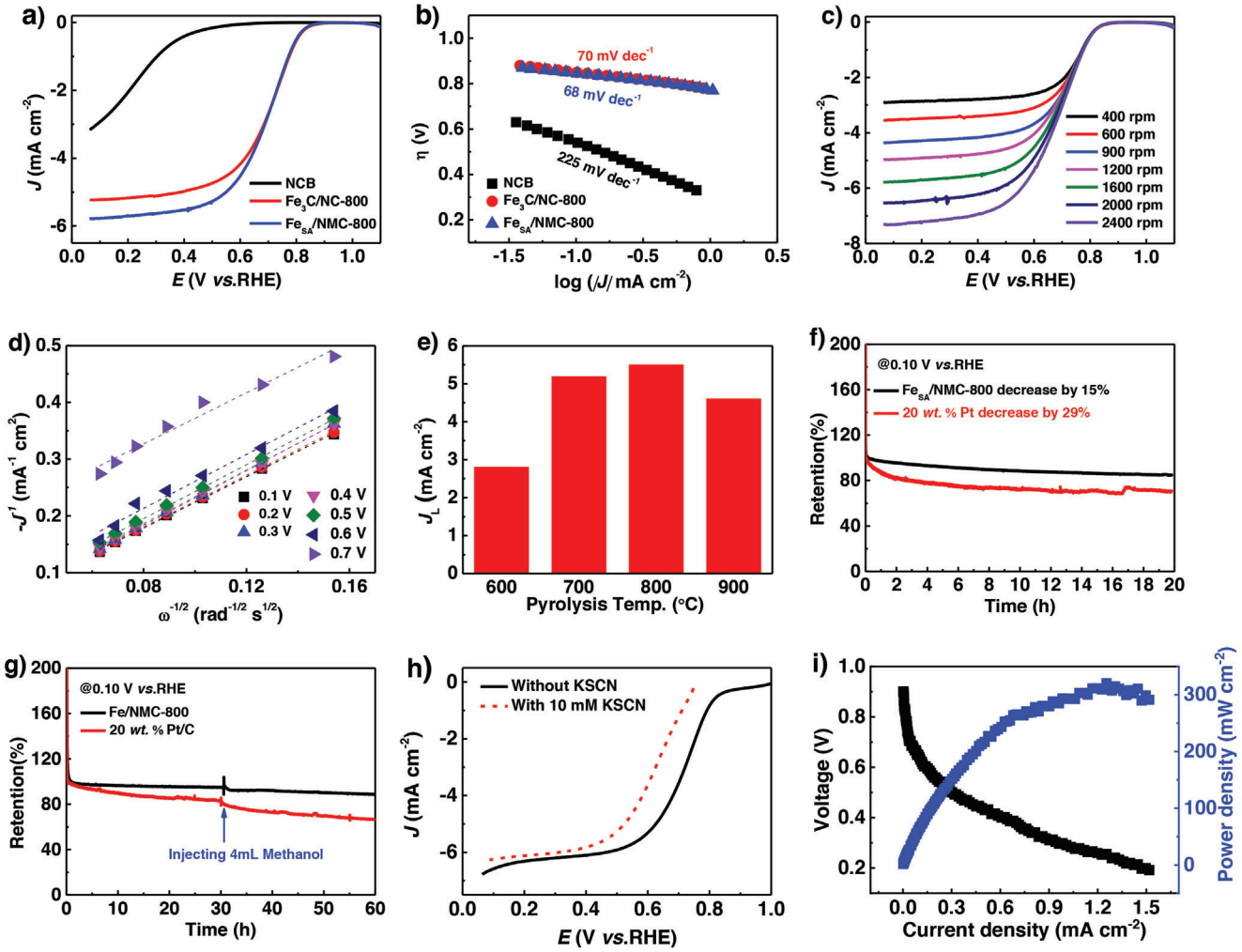

Figure 3. Electrochemical properties and electrocatalytic performances of different catalysts studied for ORR in acidic medium. a) LSV curves and b) the corresponding Tafel plots of ORR in O_2-saturated 0.1 M $HClO_4$ solution as electrocatalyzed by Fe_{SA}/NMC-800, Fe_3C/NC-800, and NCB. The curves are obtained with RDE at a speed of 1600 rpm and a sweep rate of 2 mV s^{-1}. c) LSV curves of ORR as electrocatalyzed by Fe_{SA}/NMC-800 at different speeds and d) the corresponding *K–L* plots. e) The values of J_L of ORR as a function of the pyrolysis temperature used to synthesize the materials, f) chronoamperometric curves, and g) results of the methanol crossover reaction for Fe_{SA}/NMC-800 and commercial Pt/C (20 wt%) electrocatalysts at constant potential of 0.1 V at 1600 rpm. h) LSV curves obtained for ORR as electrocatalyzed by Fe_{SA}/NMC-800 with and without 10 mM KSCN at 1600 rpm and at a sweep rate of 2 mV s^{-1} are shown. i) Polarization and power density versus current density curves for PEMFCs assembled using Fe_{SA}/NMC-800 and 40 wt% Pt/C as electrocatalysts on the electrodes. The tests are done with the following: the loading of Fe_{SA}/NMC-800 on the cathode is 4.0 mg cm^{-2}, the loading of catalyst on the anode is 0.5 mg Pt cm^{-2}, the membrane used is Nafion 211, the electrode area is 0.785 cm^{-2}, temperature is 70 °C, the relative humidity is 100%, and the pressure of O_2/H_2 is 1.0 bar.

gradually increases when more Fe^{2+} ions are used to synthesize them, or as the value of *R* increases from 1/8 to 1/2. This is because the increase in the amount of Fe^{2+} ions in the precursor results in higher values of I_D/I_G ratio (from 0.96 to 1.0) or more defect sites as well as more catalytically active single Fe sites (Table S3, Supporting Information). However, a further increase in the value of *R*, to 1/1, results in a slight decrease in current density, which is again because excessive amount of Fe^{2+} ions in the precursor does not lead to more catalytically Fe–N_4 sites, but rather to undesirable Fe aggregates/particles in the materials. So, using very high pyrolysis temperatures as well as excessive amount of Fe^{2+} ions lead to some Fe aggregates that are undesirable for electrocatalysis, which is not uncommon for such materials.[25] Regardless, all Fe_{SA}/NMC-T and Fe_{SA}/NMC-R give higher values of *n* (>3.9) and lower yields of H_2O_2 while electrocatalyzing the ORR in a wide potential range (0.07–0.8 V), as shown in Figures S23–S26 and Table S6 (Supporting Information). This demonstrates that a near 4-electron reduction pathway takes place over Fe_{SA}/NMCs during ORR in acidic media.

To assess the durability of the catalysts during electrocatalysis of ORR in acidic media, chronoamperometric curve for Fe_{SA}/NMC-800 at speed of 1600 rpm is obtained. After continuous reaction for 20 h at a constant potential of 0.1 V, the cathodic current is found to be ≈88% (Figure 3f), which is much higher than that of Pt/C (20 wt%), whose corresponding value is only ≈70% under the same condition. This shows that the catalytically active Fe–N_4 coordinated sites in Fe_{SA}/NMC-800 are more stable than Pt/C during electrocatalysis of ORR in acidic media. The

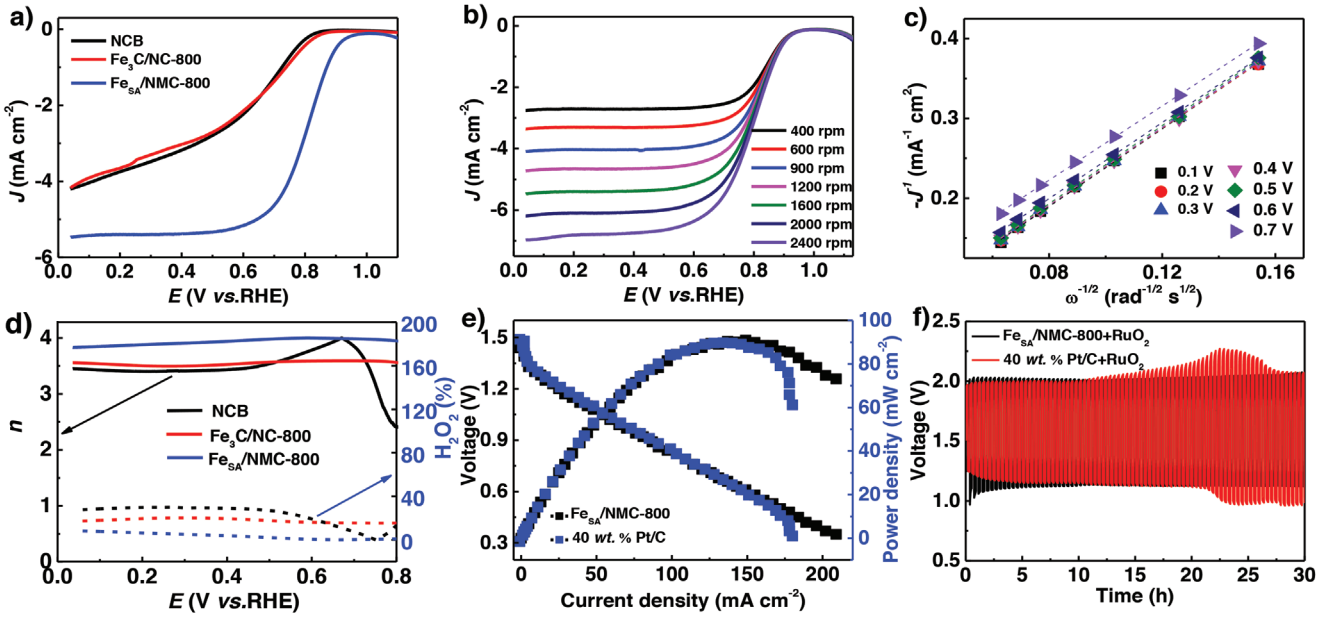

Figure 4. Electrocatalytic properties of different materials for ORR in alkaline medium. a) LSV curves of Fe_{SA}/NMC-800, Fe_3C/NC-800, and NCB acquired with a RDE at 1600 rpm and at a scan rate of 2 mV s^{-1} in O_2-saturated 0.1 M KOH solution. b) LSV curves of ORR as electrocatalyzed by Fe_{SA}/NMC-800 that are acquired with a RDE at different rotation speeds and c) the corresponding *K–L* plots. d) Graphs of the values of *n* (and the yield of H_2O_2) versus applied potential during ORR over Fe_{SA}/NMC-800, Fe_3C/NC-800, and NCB catalysts. e) Polarization and power density versus current density curves for the home-made zinc–air batteries containing Fe_{SA}/NMC-800 and Pt/C (40 wt%) at its cathode and anode electrodes, respectively. f) Galvanostatic discharge-charge cycling curves of zinc–air batteries equipped with Fe_{SA}/NMC-800 and Pt/C (40 wt%)+RuO_2 catalysts at a current density of 5 mA cm^{-2}.

TEM and elemental mapping images of the material collected after 20 h of reaction (Figure S27, Supporting Information) show no aggregated particles either, further collaborating the stability of Fe species against aggregation. Moreover, the high-resolution XPS of N 1s spectrum of the electrocatalyst after the reaction still show all five peaks associated with pyrrolic-N, pyridinic-N, graphitic-N, Fe–N, and oxidized-N species (Figure S28, Supporting Information), indicating once again the acid-resistance or stability of the Fe–N_4 moieties in the catalyst.

In addition, methanol tolerance test is conducted for Fe_{SA}/NMC-800 during ORR (Figure 3g). The result reveals that the current density of the reaction remains almost the same after introduction of 4 mL methanol (or 1.0 M methanol) into the O_2-saturated 0.1 M $HClO_4$ electrolyte . However, a significant decay in the current density is observed for Pt/C (20 wt%) under the same condition. Thus, it can be said that Fe_{SA}/NMC-800 tolerates the methanol crossover reaction better than Pt/C (20 wt%) does, which is an important property that is required of electrocatalysts to find practical applications in fuel cells. Additionally, SCN^- poisoning test is carried out by adding KSCN into the electrolyte to identify the origin of electrocatalytic activity in Fe_{SA}/NMC-800's toward ORR (Figure 3h). The electrocatalytic performance of the material significantly decreases after the addition of 11 mL of 100 mM KSCN into 0.1 M $HClO_4$ electrolyte (which means a final concentration of 10 mM). This indicates that SCN^- ions strongly bind to the Fe–N_4 sites in Fe_{SA}/NMC-800 making them inactive. This indirectly reveals the importance of atomically dispersed Fe–N_4 sites in the electrocatalytic activities and performances of Fe_{SA}/NMC-800 in ORR.[26]

Additionally, a proton exchange membrane fuel cell (PEMFC) that operates with H_2-O_2 and that contains Fe_{SA}/NMC-800 as electrocatalyst is assembled and tested to verify the material's high activity for ORR in acidic condition in practical fuel cells. The polarization and power density curves of the fuel cell, depicted in Figure 3i, show that the cell gives an open circuit voltage of 0.86 V and a maximum power density of 320 mW cm^{-2} at current density of 970 mA cm^{-2}, which are comparable with those of the reported materials (Table S6, Supporting Information). These values indicate Fe_{SA}/NMC-800's potential application in PEMFC. The stability of Fe_{SA}/NMC-800 in PEMFC device is also assessed. An initial decay in current density, which is typical to single Fe atom ORR electrocatalysts,[22] followed by relatively more stable current density, is observed (Figure S29, Supporting Information).

Next, the electrocatalytic performance of Fe_{SA}/NMCs toward ORR in O_2-saturated 0.1 M KOH solution is investigated. As shown in **Figure 4**a, Fe_{SA}/NMC-800 exhibits an excellent electrocatalytic activity for the reaction with a positive onset potential of 0.98 V and a large diffusion limited current density of 5.4 mA cm^{-2} at electrode's rotational speed of 1600 rpm. Its electrocatalytic performance in alkaline solution is also found to be much better than those of Fe_3C@NC-800 and NCB. Thus, the higher electrocatalytic activity of Fe_{SA}/NMC-800 for ORR in alkaline medium is ascribed to the atomically dispersed Fe–N_4 species as well. This is further corroborated by the small Tafel slope of 104 mV dec^{-1} obtained for it (Figure S30, Supporting Information). Moreover, this material is found to be among the best-performing single atom electrocatalysts for ORR in alkaline

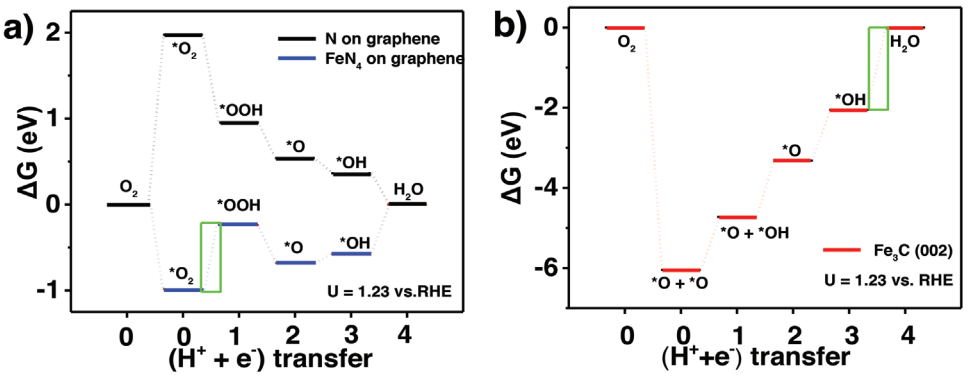

Figure 5. Free energy diagram of the transformation of O_2 to water on a) N-doped graphene and single atom FeN_4 site on graphene and b) on the (002) surface of Fe_3C.

media compared with other related systems (Table S7, Supporting Information).

The ORR over Fe_{SA}/NMC-800 is run with RDE at different rotating speeds to further study the reaction's kinetics over the catalyst in alkaline solution (Figures S31–S36, Supporting Information). By applying the *K–L* equation on the obtained LSV curves, the values of *n* of the reaction as catalyzed by the material in the potential range of 0.1–0.7 V are found to be between 3.75 and 3.90. Meanwhile, the values of *n* determined using RRDE technique at rotational speed of 1600 rpm in a large potential window of 0.1–0.8 V are found to be between 3.87 and 3.99. This means that ORR over Fe_{SA}/NMC-800 in alkaline solution also proceeds largely through 4-electron reduction pathway, yielding only a small amount of H_2O_2 (<6.8%), like the one in the acidic solution.

The stability and methanol tolerance of Fe_{SA}/NMC-800 and Pt/C (20 wt%) during ORR in alkaline medium are also investigated (Figure S37, Supporting Information). The former catalyst, once again, exhibits a much greater stability and methanol crossover resistance than the latter catalyst in alkaline electrolyte. After 20 h long test at a potential of 0.2 V and at a rotational speed of 1600 rpm in 0.1 M KOH solution, the reaction over Fe_{SA}/NMC-800 results in only a slight current loss (12%), while the one over Pt/C loses more than twice current (30%). The TEM and elemental mapping images of Fe_{SA}/NMC-800 after the durability test in alkaline solution (Figure S38, Supporting Information) display homogenously distributed Fe, N, and C atoms, with no Fe aggregates. Moreover, high-resolution XPS spectra of C 1s and N 1s of the spent catalyst (Figure S39, Supporting Information) do not appear different from those of the original catalyst. Both results corroborate the stability of the atomically dispersed Fe–N_4 present in Fe_{SA}/NMC-800 during the electrocatalytic reaction in alkaline electrolyte. Furthermore, after the addition of methanol, the current produced by ORR over Fe_{SA}/NMC-800 remains almost the same, whereas that over Pt/C (20 wt%) is lower, indicating Fe_{SA}/NMC-800's tolerance to methanol during ORR in alkaline condition. The other Fe_{SA}/NMC materials obtained at other pyrolysis temperatures and from precursors with different amounts of Fe^{2+} ions can also electrocatalyze ORR in alkaline media with values of *n* close to 4, albeit with less current density or higher onset potential than Fe_{SA}/NMC-800. All the electrocatalytic performances of the materials for ORR are compiled and presented in Table S8 (Supporting Information).

Next, a home-made zinc–air battery is assembled using Fe_{SA}/NMC-800-coated carbon paper as an air cathode and a zinc foil as an anode. For comparison, another battery with Pt/C (40 wt%) as an air cathode and zinc foil as an anode is assembled. As shown in Figure 4c, the former produces a slightly larger open-circuit voltage (OCV) (1.45 V) than the latter (1.42 V). Moreover, the former gives a peak power density of 91 mW cm^{-2} at current density of 145 mA cm^{-2}, which is comparable to that of the latter, which is 90 mW cm^{-2}, as well as the other reported ones (Table S9, Supporting Information). Additionally, there is no noticeable potential drop in the zinc–air battery during galvanostatic charge–discharge for 30 h at 5 mA cm^{-2} (Figure 4d), indicating the reversibility of charge–discharge processes during its operation. These findings confirm that Fe_{SA}/NMC-800 has an excellent electrocatalytic activity and stability to serve as an air cathode for ORR in practical rechargeable zinc–air batteries.

3. Density Functional Theory (DFT) Calculations

To deeply understand the underlying origins of the high ORR activity of Fe_{SA}/NMC-800, density functional theory (DFT) calculations are conducted. Previous reports have indicated that the potential determining step in ORR in acidic solution is the same as that in alkaline solution because the free energy change of each reaction is the same regardless of pH.[27] Hence, in this work, the calculation is only carried out for acidic solution or pH = 0. **Figure 5** displays the changes in the free energy profiles from O_2 to water in acidic media on three different catalysts, namely, single atom FeN_4 site on graphene, N-doped graphene, and Fe_3C (002) surface. The optimized structures of the surface-adsorbed reaction intermediates on (002) surface of Fe_3C, N-doped graphene, and Fe-N_4 on graphene are shown in Figure S40 (Supporting Information). Based on the results, Fe–N_4 can be said to be a more favorable site to electrocatalyze the ORR compared with the other two. The calculated results further show that the limiting potential of ORR processes on single atom Fe-N_4 site on graphene is governed by the most endothermic step, namely the formation of *OOH from adsorbed O_2. In the case of N-doped graphene, the surface of the material is not conducive to adsorb oxygen. On the contrary, the sites on Fe_3C bind the reaction intermediates

too strongly, which means that the two adsorbed oxygen atoms formed from the dissociation of surface adsorbed O_2 molecule face large energy barriers during desorption. These results overall indicate that Fe-N_4 on graphene is more active electrocatalyst than both Fe_3C and N-doped graphene.

4. Conclusions

In conclusion, high density of single Fe atoms dispersed on N-doped mesoporous carbons in form of Fe–N_4 species have been successfully synthesized by pyrolysis of Fe-chelated polypyrrole (Fe-PPY) and then etching Fe_3C byproducts from the resulting material. By varying the pyrolysis temperature and the ratio of Fe^{2+} ions:PPYe in the precursors, different materials were obtained and studied, along with relevant control material containing no Fe. The high density of Fe–N_4 sites and the mesoporous structures in the materials have allowed them to exhibit good mass transport and electrocatalytic activities toward ORR in acidic as well as in alkaline media. The most optimal electrocatalyst was found to be one that was pyrolyzed at 800 °C (Fe_{SA}/NMC-800), and it displayed an excellent electrocatalytic activity as well as long-term stability during ORR in both media. It also exhibited good performances as electrocatalyst in PEMFC and zinc–air battery, indicating its viability in practical applications in energy conversion and storage systems. The work can provide a new synthetic strategy for producing highly efficient, noble-metal-free, single atom electrocatalysts for ORR for renewable energy applications.

Supporting Information

Supporting Information is available from the Wiley Online Library or from the author.

Acknowledgements

H.X., B.D., and X.H. contributed equally to this work. The authors gratefully acknowledged the financial support from the Natural Science Foundation of Guangdong Province (Nos. 2022A1515010211 and 207078903043).

Conflict of Interest

The authors declare no conflict of interest.

Data Availability Statement

The data that support the findings of this study are available from the corresponding author upon reasonable request.

Keywords

electrocatalysis, iron, N-doped mesoporous carbon, oxygen reduction reaction, single atom catalysts

Received: April 16, 2023
Revised: April 24, 2023
Published online: May 12, 2023

[1] a) M. K. Debe, *Nature* **2012**, *486*, 43; b) K. Jiao, J. Xuan, Q. Du, Z. Bao, B. Xie, B. Wang, Y. Zhao, L. Fan, H. Wang, Z. Hou, S. Huo, N. P. Brandon, Y. Yin, M. D. Guiver, *Nature* **2021**, *595*, 361; c) Z. L. Wang, D. Xu, J. J. Xu, X. B. Zhang, *Chem. Soc. Rev.* **2014**, *43*, 7746.

[2] a) D.-W. Wang, D. Su, *Energy Environ. Sci.* **2014**, *7*, 576; b) L. Dai, Y. Xue, L. Qu, H. J. Choi, J. B. Baek, *Chem. Rev.* **2015**, *115*, 4823.

[3] a) X. Huang, Z. Zhao, L. Cao, Y. Chen, E. Zhu, Z. Lin, M. Li, A. Yan, A. Zettl, Y. M. Wang, X. Duan, T. Mueller, Y. Huang, *Science* **2015**, *348*, 1230; b) S. Guo, S. Zhang, S. Sun, *Angew. Chem., Int. Ed.* **2013**, *52*, 8526; c) M. Li, Z. Zhao, T. Cheng, A. Fortunelli, C.-Y. Chen, R. Yu, Q. Zhang, L. Gu, B. V. Merinov, Z. Lin, E. Zhu, T. Yu, Q. Jia, J. Guo, L. Zhang, W. A. Goddard, Y. Huang, X. Duan, *Science* **2016**, *354*, 1414.

[4] a) Y. Zheng, Y. Jiao, Y. Zhu, Q. Cai, A. Vasileff, L. H. Li, Y. Han, Y. Chen, S. Z. Qiao, *J. Am. Chem. Soc.* **2017**, *139*, 3336; b) Y. Chen, S. Ji, C. Chen, Q. Peng, D. Wang, Y. Li, *Joule* **2018**, *2*, 1242; c) J. Zhang, Y. Zhao, C. Chen, Y. C. Huang, C. L. Dong, C. J. Chen, R. S. Liu, C. Wang, K. Yan, Y. Li, G. Wang, *J. Am. Chem. Soc.* **2019**, *141*, 20118.

[5] a) P. Yin, T. Yao, Y. Wu, L. Zheng, Y. Lin, W. Liu, H. Ju, J. Zhu, X. Hong, Z. Deng, G. Zhou, S. Wei, Y. Li, *Angew. Chem., Int. Ed.* **2016**, *55*, 10800; b) C. Zhu, Q. Shi, B. Z. Xu, S. Fu, G. Wan, C. Yang, S. Yao, J. Song, H. Zhou, D. Du, S. P. Beckman, D. Su, Y. Lin, *Adv. Energy Mater.* **2018**, *8*, 1801956; c) M. Xiao, J. Zhu, L. Ma, Z. Jin, J. Ge, X. Deng, Y. Hou, Q. He, J. Li, Q. Jia, S. Mukerjee, R. Yang, Z. Jiang, D. Su, C. Liu, W. Xing, *ACS Catal.* **2018**, *8*, 2824; d) J. Li, M. Chen, D. A. Cullen, S. Hwang, M. Wang, B. Li, K. Liu, S. Karakalos, M. Lucero, H. Zhang, C. Lei, H. Xu, G. E. Sterbinsky, Z. Feng, D. Su, K. L. More, G. Wang, Z. Wang, G. Wu, *Nat. Catal.* **2018**, *1*, 935; e) J. Masa, W. Xia, M. Muhler, W. Schuhmann, *Angew. Chem., Int. Ed.* **2015**, *54*, 10102.

[6] a) E. F. Holby, G. Wang, P. Zelenay, *ACS Catal.* **2020**, *10*, 14527; b) X. Wan, Q. Liu, J. Liu, S. Liu, X. Liu, L. Zheng, J. Shang, R. Yu, J. Shui, *Nat. Commun.* **2022**, *13*, 2963; c) H. T. Chung, D. A. Cullen, D. Higgins, B. T. Sneed, E. F. Holby, K. L. More, P. Zelenay, *Science* **2017**, *357*, 479; d) Z. Wang, X. Jin, C. Zhu, Y. Liu, H. Tan, R. Ku, Y. Zhang, L. Zhou, Z. Liu, S. J. Hwang, H. J. Fan, *Adv. Mater.* **2021**, *33*, 2104718.

[7] a) M. Lefèvre, E. Proietti, F. Jaouen, J.-P. Dodelet, *Science* **2009**, *324*, 71; b) X. Wan, X. Liu, Y. Li, R. Yu, L. Zheng, W. Yan, H. Wang, M. Xu, J. Shui, *Nat. Catal.* **2019**, *2*, 259; c) Y. Chen, S. Ji, Y. Wang, J. Dong, W. Chen, Z. Li, R. Shen, L. Zheng, Z. Zhuang, D. Wang, Y. Li, *Angew. Chem., Int. Ed.* **2017**, *56*, 6937; d) L. Jiao, J. Li, L. L. Richard, Q. Sun, T. Stracensky, E. Liu, M. T. Sougrati, Z. Zhao, F. Yang, S. Zhong, H. Xu, S. Mukerjee, Y. Huang, D. A. Cullen, J. H. Park, M. Ferrandon, D. J. Myers, F. Jaouen, Q. Jia, *Nat. Mater.* **2021**, *20*, 1385.

[8] a) J.-C. Li, Z.-Q. Yang, D.-M. Tang, L. Zhang, P.-X. Hou, S.-Y. Zhao, C. Liu, M. Cheng, G.-X. Li, F. Zhang, H.-M. Cheng, *NPG Asia Mater.* **2018**, *10*, e461; b) K. Strickland, E. Miner, Q. Jia, U. Tylus, N. Ramaswamy, W. Liang, M. T. Sougrati, F. Jaouen, S. Mukerjee, *Nat. Commun.* **2015**, *6*, 7343; c) J.-C. Li, F. Xiao, H. Zhong, T. Li, M. Xu, L. Ma, M. Cheng, D. Liu, S. Feng, Q. Shi, H.-M. Cheng, C. Liu, D. Du, S. P. Beckman, X. Pan, Y. Lin, M. Shao, *ACS Catal.* **2019**, *9*, 5929.

[9] a) Z. Jin, P. Li, Y. Meng, Z. Fang, D. Xiao, G. Yu, *Nat. Catal.* **2021**, *4*, 615; b) X. Chen, L. Yu, S. Wang, D. Deng, X. Bao, *Nano Energy* **2017**, *32*, 353; c) X. Hai, S. Xi, S. Mitchell, K. Harrath, H. Xu, D. F. Akl, D. Kong, J. Li, Z. Li, T. Sun, H. Yang, Y. Cui, C. Su, X. Zhao, J. Li, J. Pérez-Ramírez, J. Lu, *Nat. Nanotechnol.* **2022**, *17*, 174.

[10] a) M. Lv, H. Guo, H. Shen, J. Wang, J. Wang, Y. Shimakawa, M. Yang, *Phys. Chem. Chem. Phys.* **2020**, *22*, 7218; b) X. Wei, S. Song, N. Wu, X. Luo, L. Zheng, L. Jiao, H. Wang, Q. Fang, L. Hu, W. Gu, W. Song, C. Zhu, *Nano Energy* **2021**, *84*, 105840; c) B. Y. Guan, L. Yu, X. W. Lou, *Energy Environ. Sci.* **2016**, *9*, 3092.

[11] X. Zhang, X. Han, Z. Jiang, J. Xu, L. Chen, Y. Xue, A. Nie, Z. Xie, Q. Kuang, L. Zheng, *Nano Energy* **2020**, *71*, 104547.

[12] a) S. Xu, M. Wang, G. Saranya, N. Chen, L. Zhang, Y. He, L. Wu, Y. Gong, Z. Yao, G. Wang, Z. Wang, S. Zhao, H. Tang, M. Chen, H. Gou, *Appl. Catal., B* **2020**, *268*, 118385; b) H. Wang, F. X. Yin, N. Liu, R. H.

Kou, X. B. He, C. J. Sun, B. H. Chen, D. J. Liu, H. Q. Yin, *Adv. Funct. Mater.* **2019**, *29*, 1901531.

[13] a) S. Liu, C. Li, M. J. Zachman, Y. Zeng, H. Yu, B. Li, M. Wang, J. Braaten, J. Liu, H. M. Meyer, M. Lucero, A. J. Kropf, E. E. Alp, Q. Gong, Q. Shi, Z. Feng, H. Xu, G. Wang, D. J. Myers, J. Xie, D. A. Cullen, S. Litster, G. Wu, *Nat. Energy* **2022**, *7*, 652; b) X. Ao, W. Zhang, Z. Li, J. G. Li, L. Soule, X. Huang, W. H. Chiang, H. M. Chen, C. Wang, M. Liu, X. C. Zeng, *ACS Nano* **2019**, *13*, 11853; c) H. Shen, E. Gracia-Espino, J. Ma, H. Tang, X. Mamat, T. Wagberg, G. Hu, S. Guo, *Nano Energy* **2017**, *35*, 9.

[14] a) J. Han, H. Bao, J.-Q. Wang, L. Zheng, S. Sun, Z. L. Wang, C. Sun, *Appl. Catal., B* **2021**, *280*, 119411; b) L. Deng, L. Qiu, R. Hu, L. Yao, Z. Zheng, X. Ren, Y. Li, C. He, *Appl. Catal., B* **2022**, *305*, 121058.

[15] a) Y. Xu, L. Zhu, X. Cui, M. Zhao, Y. Li, L. Chen, W. Jiang, T. Jiang, S. Yang, Y. Wang, *Nano Res.* **2020**, *13*, 752; b) E. P. Sajitha, V. Prasad, S. V. Subramanyam, S. Eto, K. Takai, T. Enoki, *Carbon* **2004**, *42*, 2815; c) A. Gomez-Martin, Z. Schnepp, J. Ramirez-Rico, *Chem. Mater.* **2021**, *33*, 3087.

[16] a) Y. Meng, D. Voiry, A. Goswami, X. Zou, X. Huang, M. Chhowalla, Z. Liu, T. Asefa, *J. Am. Chem. Soc.* **2014**, *136*, 13554; b) Y. Meng, X. Zou, X. Huang, A. Goswami, Z. Liu, T. Asefa, *Adv. Mater.* **2014**, *26*, 6510.

[17] S. Huang, Y. Meng, S. He, A. Goswami, Q. Wu, J. Li, S. Tong, T. Asefa, M. Wu, *Adv. Funct. Mater.* **2017**, *27*, 1606585.

[18] B. Ravel, M. Newville, *J. Synchrotron. Radiat.* **2005**, *12*, 537.

[19] Y. Li, X. Zhu, L. Li, F. Li, X. Zhang, Y. Li, Z. Zheng, *Small* **2022**, *18*, 2105487.

[20] J. Wang, W. Liu, G. Luo, Z. Li, C. Zhao, H. Zhang, M. Zhu, Q. Xu, X. Wang, C. Zhao, Y. Qu, Z. Yang, T. Yao, Y. Li, Y. Lin, Y. Wu, Y. Li, *Energy Environ. Sci.* **2018**, *11*, 3375.

[21] L. Zhao, Y. Zhang, L. B. Huang, X. Z. Liu, Q. H. Zhang, C. He, Z. Y. Wu, L. J. Zhang, J. Wu, W. Yang, L. Gu, J. S. Hu, L. J. Wan, *Nat. Commun.* **2019**, *10*, 1278.

[22] L. Yang, D. Cheng, H. Xu, X. Zeng, X. Wan, J. Shui, Z. Xiang, D. Cao, *Proc. Natl. Acad. Sci. USA* **2018**, *115*, 6626.

[23] a) J. Li, S. Chen, N. Yang, M. Deng, S. Ibraheem, J. Deng, J. Li, L. Li, Z. Wei, *Angew. Chem., Int. Ed.* **2019**, *58*, 7035; b) E. Luo, H. Zhang, X. Wang, L. Gao, L. Gong, T. Zhao, Z. Jin, J. Ge, Z. Jiang, C. Liu, W. Xing, *Angew. Chem., Int. Ed.* **2019**, *58*, 12469.

[24] H. Yang, Z. Li, S. Kou, G. Lu, Z. Liu, *Appl. Catal., B* **2020**, *278*, 119270.

[25] Q. He, Y. Meng, H. Zhang, Y. Zhang, Q. Sun, T. Gan, H. Xiao, X. He, H. Ji, *Sci. China Chem.* **2020**, *63*, 810.

[26] a) L. Liu, Y. Liao, S. Yue, C. Wu, Y. Chen, H. Xie, Y. Wang, *ACS Appl. Mater. Interfaces* **2022**, *14*, 42038; b) M. Liu, J. Lee, T. C. Yang, F. Zheng, J. Zhao, C. M. Yang, L. Y. S. Lee, *Small Methods* **2021**, *5*, 2001165; c) X. Luo, X. Wei, H. Wang, W. Gu, T. Kaneko, Y. Yoshida, X. Zhao, C. Zhu, *Nano-Micro Lett.* **2020**, *12*, 163.

[27] a) L. Chen, Y. Zhang, L. Dong, W. Yang, X. Liu, L. Long, C. Liu, S. Dong, J. Jia, *J. Mater. Chem. A* **2020**, *8*, 4369. b) I. C. Man, H. Y. Su, F. Calle-Vallejo, H. A. Hansen, J. I. Martínez, N. G. Inoglu, J. Kitchin, T. F. Jaramillo, J. K. Nørskov, J. Rossmeisl, *ChemCatChem* **2011**, *3*, 1159.